# Vernier Permanent Magnet Motors for Small-Size Servo Drives: A Scalability Study and Discussions

Laura Homiller
*Department of Mechanical Engineering*
*University of Wisconsin-Madison*
Madison, WI, USA
lhomiller@wisc.edu

Jixuan (Sean) Feng
*Department of Mechanical Engineering*
*The University of Texas at Austin*
Austin, TX, USA
feng.sean01@utexas.edu

Lei Zhou
*Department of Mechanical Engineering*
*University of Wisconsin-Madison*
Madison, WI, USA
lei.zhou@wisc.edu

***Abstract*—Owing to their unique advantage of high torque capability at low-speed operation, vernier permanent magnet (VPM) motors are gaining increasing attention for direct-drive robotic actuation applications. However, prior research and design efforts primarily focus on large-size VPM motors, while typical robot actuators are small in size and are typically in the fractional horsepower range. It is natural to wonder: are small-size VPM motors offering the same improvement compared to regular machines in torque density and specific torque? Aiming to answer this question, this paper provides a scalability study on the high-torque advantage of VPM motors. We developed both analytical and numerical models of a VPM motor, and designed and built a small-size, toroidal-winding VPM motor prototype to validate the models. Next, the model-predicted performances of a VPM motor and a baseline permanent magnet synchronous motor (PMSM) with varying overall sizes are presented. The scalability study shows that the benefit of VPM motors compared with PMSM is not as significant in small machines compared with larger machines, which reveals key challenges in the design and optimization of small-size VPM motors for high-performance servo applications.**

***Index Terms*—Vernier permanent magnet motor, direct-drive motor, scalability**

## I. Introduction

Driven by the advances of robotics and recent labor shortages, new installations of robots in worldwide factories and warehouses are increasing exponentially. A significant portion of this growth is in collaborative robots, or cobots, since they provide excellent safety and responsiveness needed for modern factory automation [1]. To achieve the required superior interaction capability, cobot actuators must not include transmissions with a high gear ratio. Therefore, the electric machine for cobot actuation must offer excellent torque density and specific torque to reach the desired strength while maintaining interaction capabilities. Similar actuation requirements exist in a wide range of robotic applications such as actuators for robotic hands [2] and exoskeletons [3], which calls for innovations in electric machine technology.

Among various electric machine concepts, vernier permanent magnet (VPM) machines are known for high-torque and low-ripple operation [4], [5], making them attractive for high-torque, direct-drive applications. VPM machines have drawn significant research interest in the past decades and have been investigated for various applications requiring high torque capability, including wind turbines [6]–[8], in-wheel drive for electric vehicles [9]–[14], and electric ships [15], [16]. In recent years, driven by the increasing need for robotic actuation, the high-torque benefit of VPM motors has also inspired researchers and designers to explore their applications as robotic actuators. However, to our knowledge, prior designs of VPM motors primarily focus on large-size machines. While several recent studies investigated the miniaturization of VPM motors for robotic actuators [17]–[19], to our knowledge, the scalability of the torque generation advantage of VPM motors has not been fully investigated. It is natural to wonder: can small-size VPM motors offer the same improvement compared to their PMSM counterparts in torque density and specific torque?

Aiming to provide a systematic answer to the question above, this work investigates the scalability of the torque output of VPM machines compared to a typical PMSM. Analytical and finite element (FE) models of VPM motors are developed and validated using the experimental test results of a small-size VPM motor. Next, the model-predicted motor performance of both the VPM motor and a baseline PMSM with varying overall sizes are presented. The scalability study shows that the constant airgap shear stress assumption that is often used in electric machine sizing is no longer suitable when the flux modulation effect exists in the machine, and the benefit of VPM motors is more significant at larger motor dimensions. This observation reveals key challenges in the design and optimization of small-size VPM motors for high-performance servo applications.

The rest of this paper is organized as follows. Section II presents the operating principle and an analytical model for VPM motors. Section III shows the validation of the VPM motor model using finite element (FE) simulations and experiments. Section IV presents a scalability study for the torque generation capability of VPM motors based on its analytical and FE models. Conclusions and future work are summarized in Section V.

This work is supported by USA National Science Foundation under Award #2221051 and the Wisconsin Electric Machines and Power Electronics Consortium (WEMPEC).

## II. VPM Motor Operating Principle and Analytical Modeling

This section presents the operating principle and an analytical model of the VPM motor to make the paper self-contained. The model in this section is largely based on reference [4]. The assumptions of the model include: (a) The magnetic reluctance and saturation effects of backiron are neglected. (b) The airgap length is small compared with the motor's radius. Therefore, the flux density, magnetomotive force (MMF), and airgap permeance vary only in the circumference direction, and are uniform in the radial direction. (c) Only the fundamental harmonic of magnet MMF and air gap permeance are considered, and all higher-order harmonics are ignored.

The high-torque operation of the VPM motor depends on the flux modulation effect enabled by the interaction between the stator teeth and the permanent magnet (PM) generated flux in the airgap. The fundamental-harmonic MMF generated by the PMs is calculated as

$$\mathcal{F}_{pm}(\theta_s) \approx \frac{4}{\pi}\frac{B_r h_m}{\mu_0}\cos(Z_r\theta_s - Z_r\omega_r t), \tag{1}$$

where $B_r$ is the remanence of the PMs, $h_m$ is the magnet thickness, $\mu_0$ is the permeability of free space, $Z_r$ is the number of pole-pairs in the rotor magnet array, $\theta_s$ is the angular coordinate in the stator-fixed frame, and $\omega_r$ is the angular velocity of the rotor. The airgap permeance, considering its average value and the first harmonic, can be calculated using a conformal mapping method as [4], [20]

$$P_g(\theta_s) \approx P_0 + P_1\cos(Z_s\theta_s), \tag{2}$$

where

$$P_0 = \frac{\mu_0}{g'}\left(1 - 1.6\beta\frac{b_0}{t}\right), \tag{3}$$

$$P_1 = \frac{\mu_0}{g'}\frac{4}{\pi}\beta\left(\frac{1}{2} + \frac{(b_0/t)^2}{0.78125 - 2(b_0/t)^2}\right)\sin\left(1.6\pi\frac{b_0}{t}\right), \tag{4}$$

$$\beta = 0.5 - \frac{1}{2\sqrt{1+(b_0/2g')^2}}, \tag{5}$$

where $Z_s$ is the number of stator teeth, $g'$ is the magnetic airgap length, $b_0$ is the width of the slot opening, and $t$ is the slot pitch. With (1)–(5), the airgap flux density distribution generated by the magnets is

$$\begin{aligned} B_{pm}(\theta_s) =& \mathcal{F}_{pm}(\theta_s)P_g(\theta_s) \\ \approx& B_{pm0}\cos(Z_r(\theta_s - \theta_m)) \\ &+ B_{pm1}\cos((Z_r \pm Z_s)\theta_s - Z_r\theta_m)), \end{aligned} \tag{6}$$

where $\theta_m$ is the rotor's angular position, $B_{pm0} = \mathcal{F}_{pm1}P_0$, $B_{pm1} = \frac{\mathcal{F}_{pm1}P_1}{2}$, and $\mathcal{F}_{pm1} = \frac{4}{\pi}\frac{B_r h_m}{\mu_0}$. Note that there are two terms in the air gap flux distribution (6): The $B_{pm0}$ term represents the fundamental harmonic of the PM flux, and the $B_{pm1}$ term presents the PM flux component modulated by the stator teeth.

Considering only the fundamental and slot harmonics, the winding function for one phase of the stator winding can be written as

$$\begin{aligned} N_s(\theta_s) \approx \frac{4}{\pi}k_w(&N\cos(p\theta_s) + N_{h1}\cos((Z_s - p)\theta_s) \\ &- N_{h2}\cos((Z_s + p)\theta_s)), \end{aligned} \tag{7}$$

where $N$ is the number of stator winding turns per phase per pole, $k_w$ is the winding factor, and $p$ is the number of stator pole pairs. For full-pitch concentrated windings, we have $N_{h1} = N/(Z_s/p - 1)$ and $N_{h2} = N/(Z_s/p + 1)$. The flux linkage in one phase of winding due to the PM-generated flux is

$$\lambda_s(\theta_s) = lR\int_0^{2\pi} N_s(\theta_s)B_{pm}(\theta_s)\mathrm{d}\theta_s, \tag{8}$$

where $l$ is the length of the stator stack, and $R_g$ is the radius through the center of the air gap. For VPM motors we have $Z_r = Z_s \pm p$ [21]. Assuming $Z_r = Z_s - p$ to enable useful torque generation from the slot harmonics, (8) can be written as

$$\lambda_s(\theta_s) = 4R_g l k_w(NB_{pm1} + N_{h1}B_{pm0})\cos(Z_r\theta_m). \tag{9}$$

Excited with symmetrical three-phase currents in the stator windings, the torque generated on the rotor can then be calculated as

$$T = 6lR_g N k_w Z_r I_s\left(\frac{B_{pm0}}{Z_r/p} + B_{pm1}\right), \tag{10}$$

where $I_s$ is the amplitude of the stator currents.

## III. FE Modeling and Model Validations

While the analytical VPM motor model presented in Section II is valuable for understanding the motor's general design principles and first-order behaviors, it cannot capture nonlinear effects in the motor such as magnetic saturation, eddy currents and hysteresis, and leakage effects. In order to investigate the VPM motor's scaling related to these behaviors and to validate the analytical model, we constructed two FE models for VPM motors, including one magnetostatic FE model and one transient FE model. The magnetostatic FE model uses the open-source software package FEMM [22], [23], which can capture saturation and leakage effects and allows for rapid simulation of a large number of geometries. The transient FE model, created in JMAG-Designer 22.2, is used to incorporate iron losses into the study. Figure 1 shows good agreement between the models for a range of motor sizes.

To provide experimental validation of the VPM motor models, a small-size VPM motor prototype was designed and constructed. The motor's key design parameters (defined in Fig. 2) are optimized through the FE simulations, and the results are shown in Figure 3. For the magnet dimensions and slot angle torque ripple in general increases with maximum torque. Torque output was prioritized for this prototype. Backiron thickness, slot length, and gap length were chosen to maximize torque while managing saturation. A fairly large airgap for this size motor was chosen for this prototype to

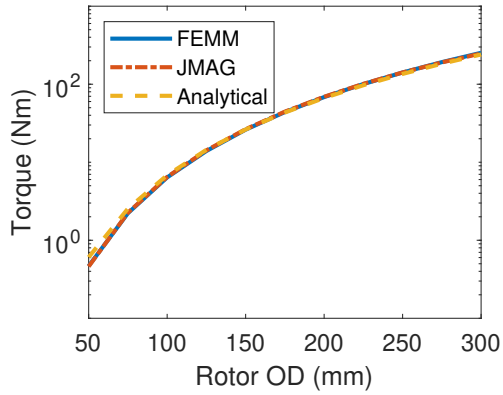


Fig. 1: Results from all three considered models, magnetostatic FE (FEMM), transient FE (JMAG), and analytical, for a range of motor sizes. Models are in good agreement.

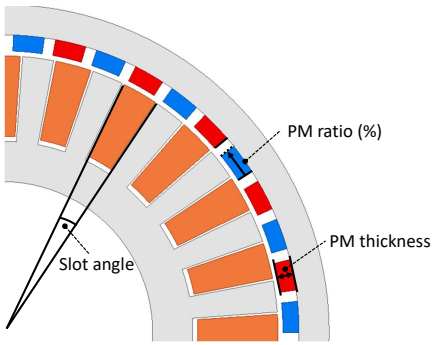


Fig. 2: Schematic for VPM motor showing parameter definitions.

ease the manufacturing process. Figure 4 shows the CAD model and photographs for the small-size VPM motor that we have constructed using the selected parameters, which features 22 PM pole pairs in the rotor and uses a toroidal winding pattern to achieve a 4-pole full-pitch winding. The prototype motor has an outer diameter of 66 mm and a 20 mm overall stack length. Preliminary testing of the machine was conducted using the setup shown in Figure 4d, where a Teknic 2310P is used as the load machine. Figure 5 shows the experimentally measured and simulated static torque-to-current relationship of the prototype motor. Good agreement validates the torque prediction accuracy of the analytical and FE models.

## IV. Model-Based Scalability Study and Discussions

### A. Shear-stress-based Scalability Discussions

This section presents a brief discussion of the sizing of electric machines based on shear stress analysis. Using the method introduced in [24, Ch. 6], the average shear stress in the airgap of an electric machine can be calculated as

$$\sigma_{avg} = \frac{\hat{B}_\delta \hat{A}_{avg}}{2}, \tag{11}$$

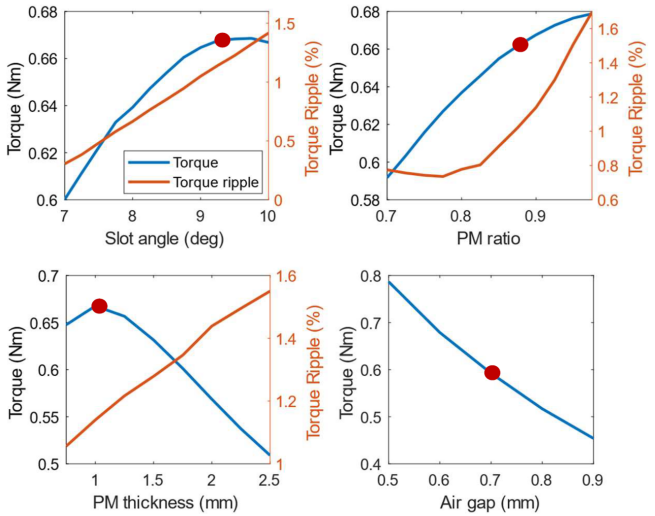


Fig. 3: FE-simulated small-size VPM motor torque and torque ripple under varied slot angle, magnet ratio, magnet thickness, and gap length. Selected parameters for the small-size VPM motor prototype are indicated by red points.

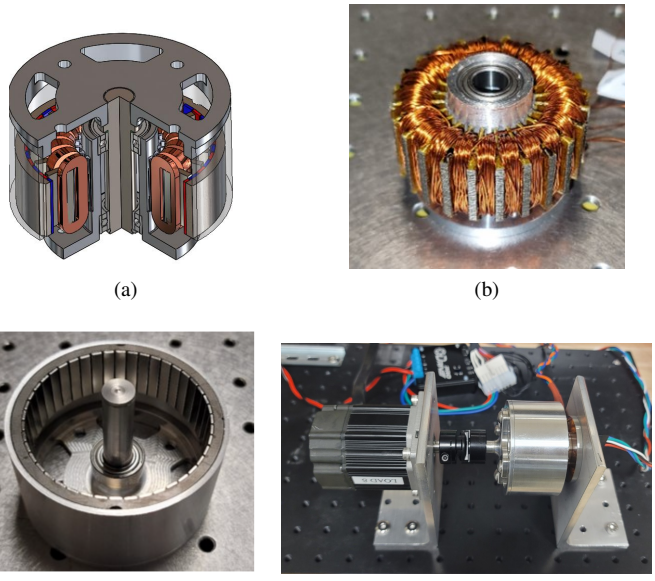

(a) (b) (c) (d)

Fig. 4: (a) CAD model of small-size VPM actuator. (b) Photo of prototype stator. (c) Photo of prototype rotor. (d) VPM motor test using a load machine (Teknic 2310P).

where $\hat{B}_\delta$ is the magnetic loading (or average airgap flux density), $\hat{A}$ is the electric loading (or peak current density). Equation (11) shows that the average shear stress is independent of the machine dimensions and geometric parameters for generating the electric and magnetic loadings in a general electric machine. Consider PMSM as an example, where the magnetic loading represents the average airgap flux density generated by the rotor magnet arrays. On the first order, $\hat{B}_\delta$ is only related to the magnet thickness and airgap length, and is not related to the machine's overall dimensions. This allows the shear stress (11) to be used for quantifying and comparing

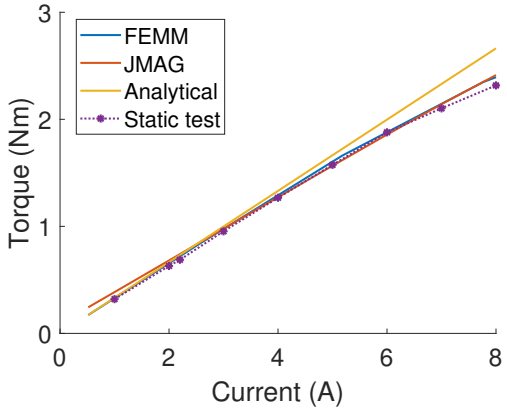


Fig. 5: Comparison between experimentally measured torque of the VPM motor prototype and simulated torque using the analytical model, magnetostatic FE model (FEMM), and transient FE model (JMAG) under varying stator currents.

the torque capability of general electric machines including PMSM.

While (11) is not dimension-relevant for most electric machines, this property does not hold for flux-modulated motors such as the VPM motors. From (3)–(5), it can be observed that the geometric parameters such as slot opening and slot pitch, and their ratio with the airgap length, can affect the magnitude of the airgap permeance, which affects the airgap flux density distribution (6), i.e., the magnetic loading. Figure 6 shows the analytically simulated air gap permeance, predicted torque, and average airgap shear stress of a VPM motor with varying rotor outer diameter 50 mm to 300 mm. Here, a stator current density of 5 A/mm$^2$ is assumed, and machine geometric parameters, including air gap length, magnetic thickness, slot length, slot opening angle, and number of pole pairs, were selected to be the same with the small-size VPM motor prototype (as shown in Fig. 3) and were held constant. It can be seen from Fig. 6 that the magnitude of both airgap permeance terms $P_0$ and $P_1$ vary with the motor's overall dimension, with $P_0$ decreasing with the rotor diameter, and $P_1$ increasing with the rotor diameter. Intuitively, as the diameter of the machine increases, so does the width of the slot openings $b_0$, which allows more air gap magnetic flux to get into the stator slots, thereby the slot harmonic of the airgap flux increases. This trend can be explained via (3) and (4): Assuming a constant magnetic air gap length, as $b_0$ increases $\beta$ will increase. The ratio between slot opening and slot pitch $b_0/t$ remains constant with motor size, so in general $P_1$ increases with outer diameter while $P_0$ decreases. In this way, the average airgap shear stress generated by the slot harmonics ($\sigma_1$ in Fig. 6) increases more than the fundamental torque ($\sigma_0$ in Fig. 6) as the machine diameter grows. This is because their corresponding airgap flux magnitude terms scale differently as the motor size varies, and the same trend is observed in their corresponding torque generation. Consequently, the total shear stress ($\sigma_{total}$) and total motor torque generation ($T_{total}$) increases with the motor size. Two conclusions can be drawn from this discussion: **(1)** The commonly used shear-stress-based sizing analysis for electric machines based on the constant airgap shear stress assumption is not suitable for VPM motors since their magnetic loading varies with the motor's overall dimension. **(2)** The total average airgap shear stress ($\sigma_{total}$) of the VPM motor increases with the motor diameter, while that of the PMSM largely holds constant as the motor size changes. Consequently, the VPM motor's torque benefit compared with regular PMSM grows as the motor size increases.

### *B. FE-model-based VPM Motor Scalability Study*

This section presents a model-based scalability study of the VPM motor in terms of torque generation compared with regular PM motors to validate the discussions presented in the section above. In this study, the detailed design parameters selected for our prototype (Fig. 4) are selected for the VPM machine being considered, and an eight-pole PMSM with the same diameter and same basic stator topology is used as a baseline. Figure 7 shows the diagrams of the motors being used in this study, and the parameters used are defined in Fig. 2. Suitable geometrical parameters were chosen to maximize torque output while minimizing torque ripple.

To investigate the scalability of the torque benefit of VPM motors compared with PMSM motors, both machines with diameters ranging from 50 mm to 300 mm were simulated using the FE models. The motor's slot length, slot opening angle, and number of pole pairs were held constant. Backiron thicknesses of both machines were chosen to keep saturation minimal in the 5 A/mm$^2$ case. Two excitation conditions were considered: assuming air-cooled machines (a typical cooling condition in cobots and robotic grippers), a 5 A/mm$^2$ current density approximates continuous operation conditions, and 10 A/mm$^2$ was used to simulate operation closer to peak torque.

Figure 8 illustrates the FE-simulated motor performances in torque (first column), specific torque (second column), torque density (third column), and average airgap shear stress (last column) under varying motor sizes. Here, the first-row data (Fig. 8a-d) shows the result with both the airgap length $g$ and the PM thickness $t_{PM}$ held constant while the motor size varies, the second-row data (Fig. 8e-h) presents the case where airgap length is held constant while PM thickness is increased linearly with motor size, and the third-row data (Fig. 8i-l) shows the situation that both airgap length and PM thickness scale proportionally with the motor's overall diameter. It can be observed from Fig. 8l that only in the last scaling case do the airgap shear stress and the torque density remain largely constant while the motor size varies. However, it is worth pointing out that this situation is not realistic in electric machine design and construction, as the airgap length does not generally scale linearly with motor size.

More realistic machine designs under varying sizes are presented Fig. 8a-d and Fig. 8e-h. Across the range of simulated sizes, the VPM motor demonstrates higher specific torque and

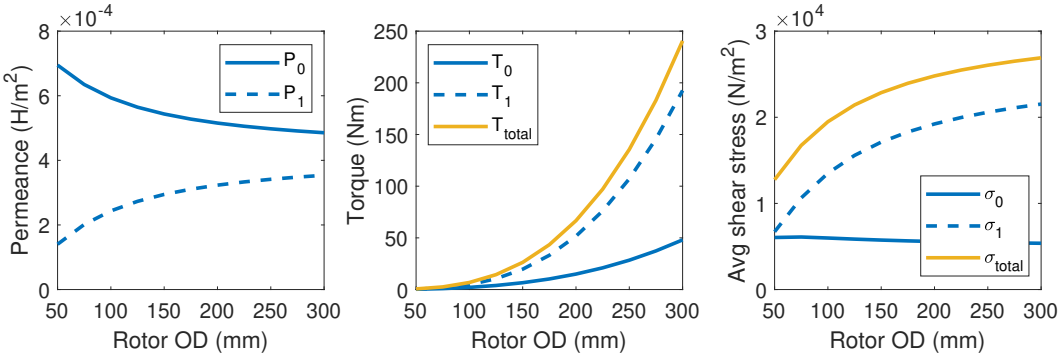


Fig. 6: Analytical model predicted airgap permeance (left), torque generation (middle), and average airgap shear stress (right) of VPM motors under varying rotor outer diameter. Here subscript "0" indicates values of the fundamental component, and subscript "1" indicates values of modulated values. The simulation is under 5 A/mm$^2$ stator current density and with constant airgap length and PM thickness.

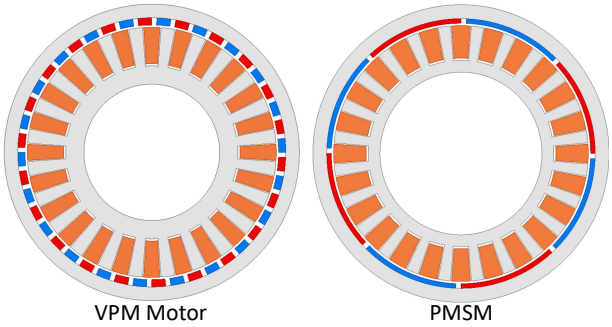


Fig. 7: Schematics for VPM motor (left) and PMSM (right) being used for FE-model-based scalability study.

torque density as predicted. However, as is shown in Fig. 8d, the airgap shear stress in a regular PMSM machine is largely constant while holding airgap size, magnet thickness, and current density constant, but there is a significant variation in airgap shear stress in VPM motors. For example, as is shown in Fig. 8d, in a PMSM motor, the average shear stress in a PMSM motor is approximately $8.5\ \mathrm{kN/m^2}$ for motors with diameters ranging from 100 to 300 mm. However, in a VPM motor with 300 mm overall diameter, the airgap stress is about $46.7\ \mathrm{kN/m^2}$ under $10\ \mathrm{A/mm^2}$ excitation, while in a 50 mm diameter VPM motor it is only $19.6\ \mathrm{kN/m^2}$. This observation is confirming our analytical-model-based discussions presented in Section IV-A, where the torque generation contribution of the modulated flux component scales with the motor size, and the torque generation due to the fundamental flux component remains largely constant as the motor size varies. This observation confirms that the commonly used constant shear stress assumption in machine scalability studies cannot be readily applied to flux-modulated machines such as VPM motors, and the scaling of stator teeth as modulators must be considered when investigating VPM motors over varying sizes.

Comparing the orange curves (PMSM data) and blue curves (VPM motor data) between the first two rows in Fig. 8, it can be observed that when PM thickness increases with motor size, the VPM specific density is about 2.5× that of the PMSM for a 50 mm diameter, and increases up to a 5× improvement for the 300 mm motors. The VPM motor does reach a higher total output torque and specific torque when the PM thickness is allowed to increase, but significant performance improvements over the PMSM can be achieved even if the PM thickness is kept small. This is because VPM motors rely on the flux modulation effect from the stator teeth, and increasing the magnet thickness can increase the motor's effective air gap size, reducing the magnitude of the modulated flux. This discussion reveals another benefit of the VPM motors in reducing the need for rare-earth permanent magnet materials compared with PMSM machines.

## V. Conclusions and Future Work

In this paper, a model-based scalability study for VPM motor's torque generation advantage is presented. This study reveals that the commonly used shear-stress-based electric machine sizing analysis is not suitable for VPM motors since the modulated airgap flux increases with the motor dimension. Since the airgap shear stress of VPM motors is reduced in small-size machines, their torque enhancement relative to PMSM is attenuated compared with their larger-size counterparts. This observation, together with additional challenges in cooling and manufacturing processes, makes the miniaturization of VPM motors for high-performance servo drives more challenging than simply scaling a large-size, high-performance VPM machine design. Future studies in innovative machine topology are suggested to overcome these obstacles to unlock the wide application of VPM motors in high-strength and interactive robotic applications.

## References

[1] "Collaborative robot market," https://www.marketsandmarkets.com/Market-Reports/collaborative-robot-market-194541294.html, accessed: March 2024.

[2] A. Bhatia, A. M. Johnson, and M. T. Mason, "Direct drive hands: Force-motion transparency in gripper design," in *Robotics: science and systems*, 2019.

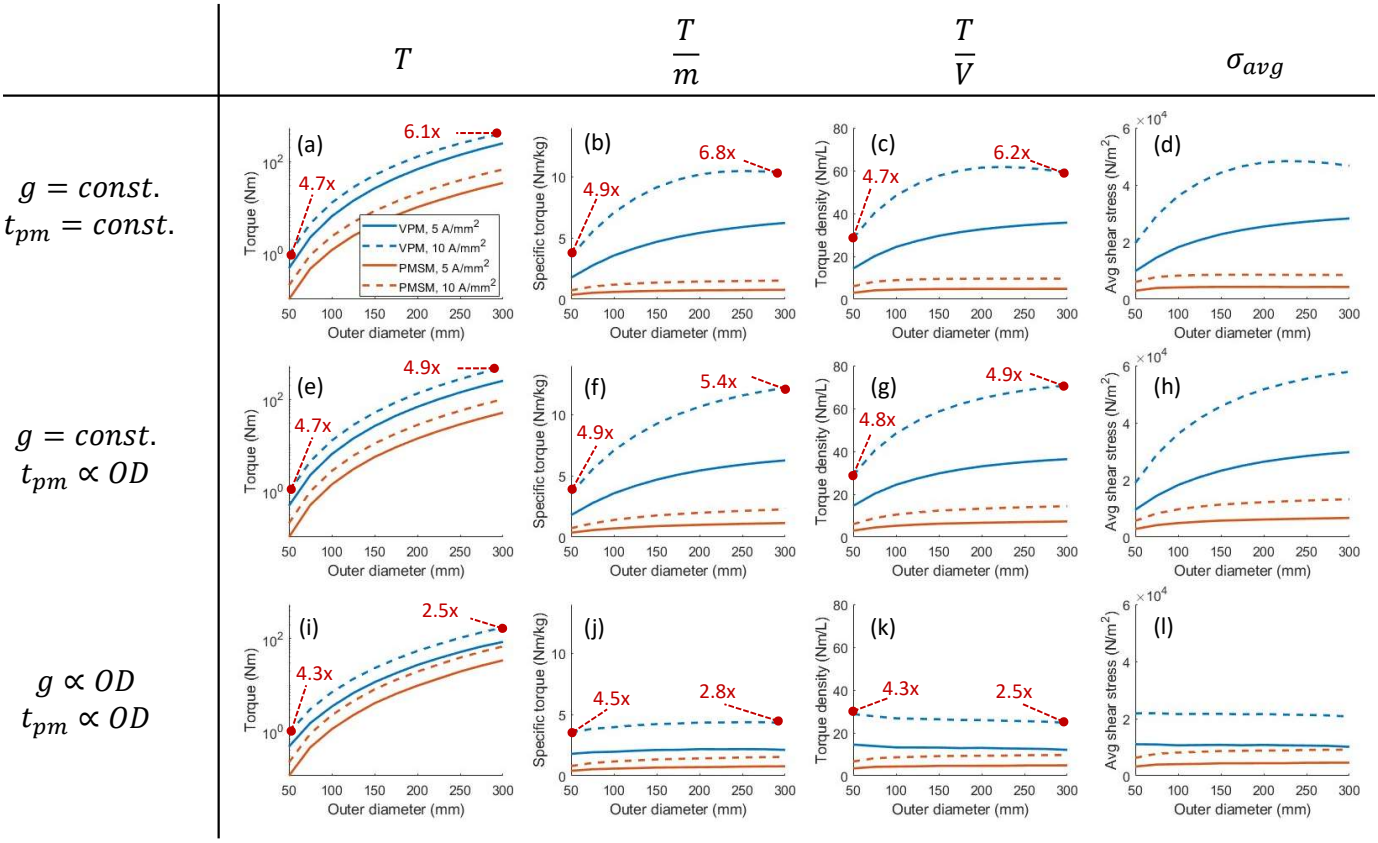


Fig. 8: Performance of the VPM motor compared to PMSM for outer diameters from 50 mm to 300 mm. (a)-(d) simulates constant airgap and constant PM thickness. (e)-(h) simulates constant airgap and PM thickness scaled with diameter. (i)-(l) simulates both airgap and PM thickness scaled with diameter.


[3] R. Gopura, K. Kiguchi, and D. Bandara, "A brief review on upper extremity robotic exoskeleton systems," in *2011 6th international Conference on Industrial and Information Systems*. IEEE, 2011, pp. 346–351.

[4] D. Li, R. Qu, J. Li, L. Xiao, L. Wu, and W. Xu, "Analysis of torque capability and quality in vernier permanent-magnet machines," *IEEE transactions on industry applications*, vol. 52, no. 1, pp. 125–135, 2015.

[5] B. Kim and T. A. Lipo, "Operation and design principles of a pm vernier motor," in *2013 IEEE Energy Conversion Congress and Exposition*. IEEE, 2013, pp. 5034–5041.

[6] B. Kim, "Design of a direct drive permanent magnet vernier generator for a wind turbine system," in *2018 IEEE Energy Conversion Congress and Exposition (ECCE)*. IEEE, 2018, pp. 4275–4282.

[7] ——, "Design method of a direct-drive permanent magnet vernier generator for a wind turbine system," *IEEE Trans. on Industry Applications*, vol. 55, no. 5, pp. 4665–4675, 2019.

[8] M. M. Derakhshani, M. Ardebili, M. Cheraghi, and R. Jafari, "Investigation of structure and performance of a permanent magnet vernier induction generator for use in double-turbine wind systems in urban areas," *IET Renewable Power Generation*, vol. 14, no. 19, pp. 4169–4178, 2020.

[9] J. Li, D. Wu, X. Zhang, and S. Gao, "A new permanent-magnet vernier in-wheel motor for electric vehicles," in *2010 IEEE Vehicle Power and Propulsion Conference*. IEEE, 2010, pp. 1–6.

[10] H. Yang, H. Lin, Z. Zhu, S. Fang, and Y. Huang, "Novel flux-regulatable dual-magnet vernier memory machines for electric vehicle propulsion," *IEEE Transactions on Applied Superconductivity*, vol. 24, no. 5, pp. 1–5, 2014.

[11] Y. Oner, Z. Zhu, and W. Chu, "Comparative study of vernier and interior pm machines for automotive application," in *2016 IEEE Vehicle Power and Propulsion Conference (VPPC)*. IEEE, 2016, pp. 1–6.

[12] R. Qu, D. Li, Y. Gao, and T. Zou, "Comparison of surface pm vernier motors with interior pm motors for traction application," in *2017 IEEE Transportation Electrification Conference and Expo, Asia-Pacific (ITEC Asia-Pacific)*. IEEE, 2017, pp. 1–6.

[13] C. H. Lee, M. Angle, K. K. Bhalla, M. Qasim, J. Mei, S. Mohammadi, K. Iyer, J. J. Sinkular, and J. L. Kirtley, "Quantitative comparison of vernier permanent-magnet motors with interior permanent-magnet motor for hybrid electric vehicles," *Energies*, vol. 11, no. 10, p. 2546, 2018.

[14] D. Wu, Z. Xiang, X. Zhu, L. Quan, M. Jiang, and Y. Liu, "Optimization design of power factor for an in-wheel vernier pm machine from perspective of air-gap harmonic modulation," *IEEE Transactions on Industrial Electronics*, 2020.

[15] J. Li and K. Chau, "A novel HTS PM vernier motor for direct-drive propulsion," *IEEE transactions on applied superconductivity*, vol. 21, no. 3, pp. 1175–1179, 2010.

[16] W. Li, T. Ching, K. Chau, and C. H. Lee, "A superconducting vernier motor for electric ship propulsion," *IEEE Trans. on Applied Superconductivity*, vol. 28, no. 3, pp. 1–6, 2017.

[17] K. SUZUKI, Y. KATAOKA, and Y. ANAZAWA, "A study of high torque design in small-size pm vernier motor," in *2020 23rd International Conference on Electrical Machines and Systems (ICEMS)*. IEEE, 2020, pp. 1872–1877.

[18] L. Zhou, F. Guo, H. Wang, and B. Wang, "High-torque direct-drive machine with combined axial-and radial-flux out-runner vernier permanent magnet motor," in *2021 IEEE International Electric Machines & Drives Conference (IEMDC)*. IEEE, 2021, pp. 1–8.

[19] M.-T. Duong, T.-P. Luu, T. D. Do, and Y. Perriard, "Design of high torque density permanent magnet motors and drives for collaborative robot applications," in *2021 24th International Conference on Electrical Machines and Systems (ICEMS)*. IEEE, 2021, pp. 1060–1064.

[20] Z. Zhu and D. Howe, "Instantaneous magnetic field distribution in brushless permanent magnet dc motors. iii. effect of stator slotting," *IEEE transactions on magnetics*, vol. 29, no. 1, pp. 143–151, 1993.

[21] A. Toba and T. A. Lipo, "Generic torque-maximizing design methodology of surface permanent-magnet vernier machine," *IEEE transactions on industry applications*, vol. 36, no. 6, pp. 1539–1546, 2000.

[22] D. Meeker, *Finite Element Method Magnetics: Version 3.4: User's Manual*. L'autor, 2004.

[23] R. Crozier and M. Mueller, "A new matlab and octave interface to a popular magnetics finite element code," in *2016 XXII International Conference on Electrical Machines (ICEM)*. IEEE, 2016, pp. 1251–1256.

[24] J. Pyrhonen, T. Jokinen, and V. Hrabovcova, *Design of rotating electrical machines*. John Wiley & Sons, 2013.